5-2019

HYDRODYNAMIC MOTION OF ELECTRON BEAM HEATED WARM DENSE MATTER

Payson Coy Dieffenbach
University of Tennessee, pdieffen@vols.utk.edu

To the Graduate Council:

I am submitting herewith a thesis written by Payson Coy Dieffenbach entitled "HYDRODYNAMIC MOTION OF ELECTRON BEAM HEATED WARM DENSE MATTER." I have examined the final electronic copy of this thesis for form and content and recommend that it be accepted in partial fulfillment of the requirements for the degree of Master of Science, with a major in Nuclear Engineering.

David Donovan, Major Professor

We have read this thesis and recommend its acceptance:

Maik Lang, Zhili Zhang, Joshua E. Coleman

Accepted for the Council:
Dixie L. Thompson

Vice Provost and Dean of the Graduate School

(Original signatures are on file with official student records.)

HYDRODYNAMIC MOTION OF ELECTRON BEAM HEATED WARM DENSE MATTER

A Thesis Presented for the
Master of Science
Degree
The University of Tennessee, Knoxville

Payson Coy Dieffenbach
May 2019

ABSTRACT

The hydrodynamic motion of warm dense matter produced by intense electrons is being experimentally studied on the Dual-Axis Radiographic Hydrodynamic Test Facility (DARHT). Experimental results are compared to hydrodynamic simulation codes for verification. Copper and titanium foils of varying thickness are heated in two stages, the first being isochoric, by an electron bunch with ~100 ns pulse length, energy of 19.8 MeV, current of 1.7 kA, and beam spot size of 2 mm. Aluminum, nickel, and carbon are heated in a similar fashion, but with a current of ~1.44 kA and beam spot size of 1 mm. The corresponding hydrodynamic motion of the foils during energy deposition is measured instantaneously with photonic Doppler velocimetry (PDV). The PDV diagnostic provides time-resolved measurement of the foil velocity, inferred pressure in the foil, and hydrodynamic disassembly time. The 1-D hydrodynamic HELIOS-CR code models the electron energy deposition on these foils. Calculated results of foil velocity and plasma pressure profiles are then compared to experimental results and 2-D hydrodynamics simulations with LASNEX. These parametric studies are crucial in understanding the evolution of warm dense matter during energy deposition, and optimizing electron-target interactions that improve the Bremsstrahlung targets and radiographic spot size capabilities on DARHT.

TABLE OF CONTENTS

LIST OF TABLES

LIST OF FIGURES

LIST OF ACRONYMS

BBU – Beam Breakup

BPM – Beam Position Monitor

DARHT – Dual-Axis Radiographic Hydrodynamic Test Facility

EOS – Equation-of-State

FWHM – Full Width at Half Maximum

HEDP – High Energy Density Physics

KE – Kinetic Energy

LTE – Local Thermodynamic Equilibrium

MTF – Modulation Transfer Function

OTR – Optical Transition Radiation

PDV – Photonic Doppler Velocimetry

S/N – Signal to Noise

VISAR – Velocity Interferometer System for Any Reflector

WDM – Warm Dense Matter

XRTS – X-Ray Thomson Scattering

CHAPTER ONE – INTRODUCTION

1.1 Background Information

As the nation's stockpile ages, a greater chance of weapon failure and unpredictability becomes more apparent with each passing year. Fissile material used in the stockpile decays over time, and electronic components suffer from the long-term radiation exposure. With full-scale tests banned in 1992, it has become a crucial mission to ensure the effectiveness and reliability of the nation's stockpile. The nation accomplishes stockpile maintenance through reliance on scaled experiments and simulations that support the Stockpile Stewardship Program. A particular tool critical to this mission is the Dual-Axis Radiographic Hydrodynamic Test Facility (DARHT) that conducts scaled hydrotests.

DARHT consists of two linear-induction electron accelerators orthogonal to one another, which are Axis-1 and Axis-2. The main difference between the two axes is that Axis-1 is a single pulsed device, and Axis-2 is a multi-pulsed device that allows for time-resolved radiography. The two axes can fire simultaneously during a hydrotest to allow for 3-D reconstruction during one time slice, or they may fire individually. The work and acquired data entailed in this document comes from experiments conducted on Axis-1 only, and thus the remaining text will focus on DARHT Axis-1.

A 100-ns-long electron bunch on Axis-1 is accelerated and focused onto a 1-mm-thick Ta target converting the particle beam energy into Bremsstrahlung radiation. The high-energy Bremsstrahlung tail penetrates thick, dense hydrotests occurring at the convergence of the two accelerators. The accelerator radiographic times are synchronized with at least 4 events in the hydro tests in order to produce time-resolved radiographs, or cross-sectional images of the hydro test. These radiographs are then compared extensively to hydrodynamic codes to cross-reference and validate the simulations. These codes, essential in validating the effectiveness of the stockpile, are being developed to simulate full-scale tests.

At DARHT, there is a need to continually improve the radiographic quality. The spot size and the intensity (dose) of the radiation governs the quality of the radiograph. In order to improve the radiographic quality, one must fully understand the interactions

between the Bremsstrahlung target and the relativistic electrons. To fully understand the evolution of the target during energy deposition, the equation of state (EOS) of the material must be known. The equation of state for a material relates the functions of state under certain physical conditions to one another. To describe the EOS, one needs three thermodynamic values such as the pressure, temperature, and density. In this document, it will be shown the photonic Doppler velocimetry (PDV) diagnostic provides temporal measurements of pressure in the foil targets during energy deposition. Further UV and X-ray spectroscopy diagnostics will be fielded on DARHT to obtain the needed measurements of temperature and density during the warm dense phase to describe the target EOS. This will lead to the optimization of the energy deposition process, and increase the radiographic capability of DARHT.

1.2 Project Objectives

The hydrodynamic motion of the foils during energy deposition is being studied with PDV measurements and concurrent simulations with the 1-D hydrodynamic code HELIOS-CR. In order to surmount the task, key objectives were identified to drive the motivation and success of this study. The objectives of this study include:

1. *Accurately extract time-resolved values of foil velocity, pressure, temperature, and hydrodynamic disassembly time from the PDV data.*
2. *Simulate the foil motion with DARHT beam parameters using a 1-D hydrodynamics code and extract key values mentioned in objective 1.*
3. *Compare experimental and simulation results to check the validity of the hydrodynamic codes for future applications.*

Completing each of these tasks allowed the project to be fully realized, and laid the groundwork for future experiments and simulations.

CHAPTER TWO – LITERATURE REVIEW

2.1 The Warm Dense Matter Regime

2.1.1 The Coupling and Degeneracy Parameters

Warm dense matter (WDM), an interesting regime in temperature and density space, covers a range of $0.1 < T(eV) < 10$ and $0.1\rho_o < \rho(cm^{-3}) < 10\rho_o$ for most metals where ρ_o is solid density. An example of this range in phase space is illustrated in figure 2.1 where the degeneracy and coupling parameters are shown [1]. Figure 2.1 illustrates that the degeneracy parameter varies by 2 orders of magnitude, and the coupling parameter varies by approximately 10x in this regime. WDM is not described well with normal condensed matter physics nor weakly-coupled plasma physics because it is too energetic and dense. It is essentially a state of matter where the ions strongly couple to one another, and partially degenerate electrons may exist. The WDM regime has gained considerable interest because there exist many astrophysical systems, brown dwarfs and the interior of gas giants, that fall into the regime. Additionally, many inertial fusion plasmas that traverse through the stages of compression go through the warm dense phase [2]. There exists an opportunity to develop experiments and models that will aid in our improved understanding of the WDM regime where data is currently limited or non-existent [3].

The strong coupling parameter relates the interatomic potentials between particles and thermal energies of these particles denoted by equation 2.1.

$$\Gamma = \frac{q^2\left(\frac{4\pi n_e}{3}\right)^{\frac{1}{3}}}{4\pi\varepsilon_o(T_e+E_F)}, \qquad \text{Equation 2.1}$$

where q is the elementary charge, and E_F is the Fermi energy calculated by $E_F = \frac{\hbar^2}{2m_e}(3\pi^2 n_e)^{\frac{2}{3}}$. When $\Gamma << 1$, the system is weakly coupled which indicates that the particles have large amounts of kinetic energy. When $\Gamma >> 1$, the system is strongly coupled and the interparticle potentials largely affect the behavior of the individual particles. In the WDM regime, $\Gamma \sim 1$, meaning that the interatomic potentials and kinetic energy are similar to one another.

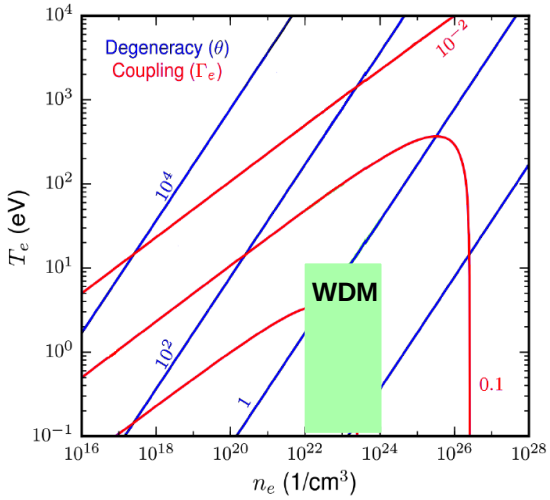

Figure 2.1: Phase diagram with labeled degeneracy and strong coupling parameters. The WDM region for most metals is shown.

The degeneracy factor, Θ, describes the ratio of the thermal energy to the Fermi energy, and ranges from 10^{-3} for high density, low temperature plasma to 10 for low density, high temperature plasma. The degeneracy factor is outlined by equation 2.2.

$$\Theta = \frac{T_e}{E_F}, \qquad \text{Equation 2.2}$$

For $\Theta >> 1$, the system is considered non-degenerate and the quantum effects associated with electrons can be neglected. For $\Theta << 1$, the system is degenerate, and the quantum effects associated with electrons must be considered [4]. With both of these factors describing the WDM regime, it has become particularly difficult to model theoretically and computationally since the methods used in conventional plasma physics are no longer valid.

2.1.2 Methods of Producing WDM

There are many methods of producing WDM through photon heating, laser-accelerated ion sources, and particle beam driven experiments. In experiments that look to produce WDM, uniformity of heating in an isochoric process is crucial to study the regime's properties efficiently. Isochoric heating occurs when the target does not expand hydrodynamically during energy deposition, and thus considered a constant volume process. The isochoric heating process on DARHT is explained more thoroughly in Section 2.3.2.

The goal of facilities that produce WDM is to offer a flexible range of abilities [3]:

- *Precisely control energy deposition with uniformity.*
- *Produce large sample sizes of considerable volume of WDM.*
- *Offer a low-debris and background radiation environment.*
- *Offer high shot rates with access to multiple target chambers.*
- *Be accessible to university students and scientists; and have technical support for experimental endeavors.*

Facilities that can meet one or more of these goals offer a pathway for researchers to gain valuable knowledge into WDM production and its evolution in time. These facilities will also offer the ability to look into the EOS of materials that are of vital importance in the inertial fusion and stockpile community.

The majority of WDM experiments are laser-driven, and involve a short (ps to tens of fs) laser pulse to rapidly heat matter. The interaction is fast and strong enough to ionize the target atoms, and the ions and electrons gain large amounts of kinetic energy. However, in direct laser heating experiments most of the laser pulse energy couples to the surface electrons and is nonuniform in its heating ability. The rest of the target is heated by the hot electrons that are produced and the return currents of cold electrons. In previous experiments, a 70-nm-thick Cu foil was irradiated with a fs Ti:Saph laser, and Cu L-shell photons were used to probe the resulting plasma to quantify the electron-ion relaxation and temperature of ~0.1 eV [5, 6].

In laser-driven ion experiments, ions are accelerated to sufficiently high kinetic energies (> 1 MeV) with the use of lasers, and directed towards targets for heating [7]. The ions transfer most of their energy to the target atoms through collisional stopping power. This heating is rapid enough that the target does not hydrodynamically expand, and is thus considered to be isochoric. However, this heating method lacks uniformity since typical laser-accelerated ion beams possess an exponential energy spread. A large number of low-energy ions are usually present in these beams, and thus result in additional heating to the front surface of the target. Previous experiments have shown laser-accelerated ion heating of carbon, gold, and diamond samples [8, 9].

The unique heating method used on DARHT is a particle beam driven approach. DARHT achieves isochoric heating through its monochromatic intense relativistic electron bunch with the ability to generate large, homogenous volumes of WDM that is both long-lasting and stable [10]. It has been shown previously that production of a large volume (3 x 10^{-4} cm^3) and mass (2.8 mg) of warm dense copper was achieved with the relativistic electron beam heating method on DARHT. This is accomplished by accelerating and transporting a 100-ns-long electron bunch through Axis-1 to 19.8 MeV. The electron bunch is then focused onto range-thin foils of approximately 100 μm thickness to a spot size of ~1 mm FWHM. Range-thin foils have been chosen to optimize isochoric heating, uniformity of heating, and to minimize resulting Bremsstrahlung production. Considering the goals outlined above, DARHT provides the ability to obtain precise control of energy deposition and uniformity of heating, produce large samples of WDM, and offer high shot rates that are repeatable.

2.1.3 Measuring the Equation of State

The purpose of WDM experiments on DARHT is two-fold: the first is to quantify the EOS of the DARHT target materials during the beam pulse and second demonstrate a capability to measure the EOS for a range of experimental conditions and materials. The goal of the first purpose is to provide insight to improve radiographic quality in the future. In order to quantify the EOS of a material in the warm dense regime, the plasma properties of electron temperature (T_e), electron density (n_e), and the pressure (P) must be measured. Ideally, a suite of diagnostics would be fielded on DARHT that would provide temporal information for all three quantities, and an EOS model could be evaluated for the relevant target material. Ultraviolet (UV) and X-ray Thomson Scattering (XRTS) diagnostics are being explored to provide time- and spatially-resolved measurements of the electron density, temperature, as well as the charge state. XRTS is a powerful, yet complicated diagnostic and has been implemented on many high-energy density plasma (HEDP) experiments [11]. The difficulties in implementing the XRTS diagnostic are attributed to the experimental setup, production of keV class X-rays to probe the target region, as well as obtaining sufficient photons on the detector for usable S/N ratios. If correctly fielded, though, it can

provide accurate measurements of the aforementioned quantities as a function of time. The effectiveness of the UV diagnostic would depend on the opacity of the plasma produced, and the opacity will vary with n_e and T_e. Spatial and temporal measurements of the emitted UV spectra may be possible, but this will be determined by proof-of-principle measurements of the UV radiation and opacity.

Many diagnostics are implemented on DARHT that include fast visible imaging, visible spectroscopy, PDV, and rough measurements of the scattered electron and Bremsstrahlung distribution. Plume velocity and expansion has been characterized previously with single gated images utilizing a PI-Max and multiple fast-frame images utilizing a Simacon camera with gates from 20 ns to 1 μs [12]. Here, visible spectroscopy measurements, modeled with the ATOMIC code, for Ti yielded the measurement for the electron temperature and density. PDV, as shown in this document, provides a wealth of information that includes the foil velocity, hydrodynamic disassembly time, and the inferred plasma pressure – one of the necessary quantities for the EOS.

2.2 The Dual-Axis Radiographic Hydrodynamic Test Facility

2.2.1 The Radiographic Mission

The objective of DARHT is to provide time resolved radiographs of hydro tests for the U.S. government, which validates the simulation accuracy of the nuclear stockpile. DARHT is a Bremsstrahlung device, consisting of two linear induction accelerators that are orthogonal to one another. An intense pulse of relativistic electrons is transported down each beamline to high-Z targets, and through the interactions of the electrons and target nuclei, produce high-doses of Bremsstrahlung radiation. The Bremsstrahlung continuum on Axis-1, shown in figure 2.2, has energies up to the operating energy of the machine, which is 19.8 MeV. An electron bunch with 10^{14} e^- will typically yield ~10^{11} γ at the Bremsstrahlung target with a 10^{-3} conversion efficiency. This braking radiation penetrates dense, scaled hydrotests that occur at the convergence of the two accelerators, and radiographic images are produced of the implosions. The two axes allow for reconstruction of 3-D radiographic images, as well as time-resolved radiographic capabilities.

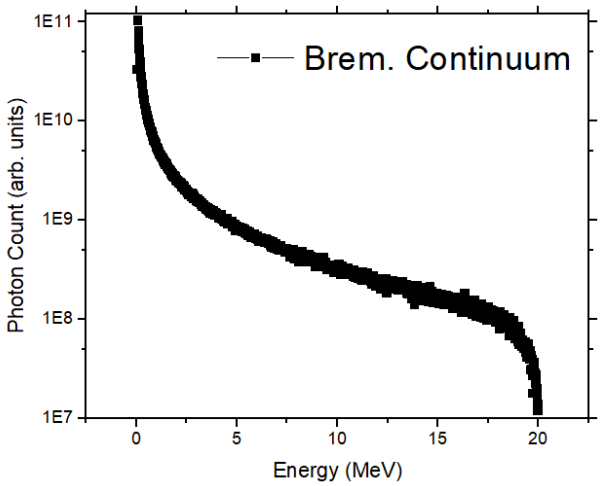

Figure 2.2: Characteristic Bremsstrahlung continuum produced at the Axis-1 conversion target.

It is currently the world's leading pulsed Bremsstrahlung device for its radiographic quality, high dose, and shot rate.

Figure 2.3 is an example of a false radiographic image produced on DARHT. These radiographs capture the hydrodynamic behavior of the hydrotest, and validate the physics models incorporated into weapons codes. The radiographic quality on DARHT will ultimately depend on the spot size of the focused electron bunch on the target, similar to the properties of a pinhole camera. Los Alamos characterizes the radiographic spot size by comparing the modulation transfer function (MTF) of the spot with the MTF of a disk that is illuminated uniformly [13]. The spot size is then defined as the diameter of the disk that has the same MTF half width as the spot of the source. The temporal resolution of the image will be governed by the motion blur of the hydrotest, and the spatial resolution will be governed by the radiographic spot size on the Bremsstrahlung target [14]. The temporal resolution of the radiograph can be improved by providing additional dose, or charge, at different time slices. This change in beam parameters will have to abide by the limits of space charge effects. As mentioned previously, the spatial resolution of the radiograph is improved by decreasing the spot size of the electron beam at the target. However, this spot size reduction will be limited by the factors such as emittance growth, beam instabilities, and electron interactions with the WDM produced at the targets. Understanding the

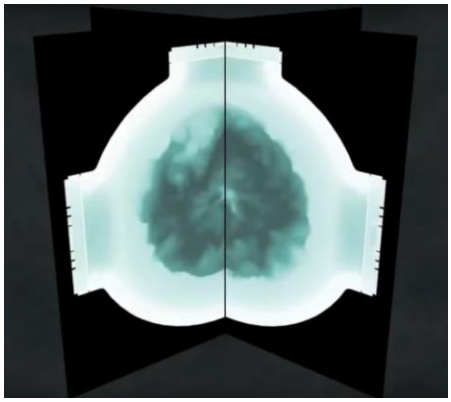

Figure 2.3: A false example of a DARHT radiographic image produced during a hydrotest.

production and evolution of the WDM at the targets during energy deposition allows optimization of radiographic quality and repeatability. Further discussion about the electron beam interactions with WDM is outlined in section 2.2.3.

A secondary goal of DARHT is to maximize the dose with a minimal spot generated during the beam-target interaction. To meet the mission of producing a quality radiograph, a dose of ~500 Rad, 1 m from the target in ~60 ns is sufficient enough to image most objects [15]. This is achieved by focusing the intense relativistic electron bunch to a source size of < 1 mm FWHM on Axis-1. With a 19.8 MeV energy limit of the device, high dose is achieved through a high beam current of kA range since dose is related to the total charge on the target and electron beam. It should be noted that the dose produced during the pulse varies in time, and peaks during the flat top region of the characteristic DARHT pulse [16].

2.2.2 DARHT Axis-1 Accelerator Layout

The Dual-Axis Radiographic Hydrodynamic Test Facility was conceived and planned in the early 1980's [17]. An aerial view of the completed DARHT facility is shown in figure 2.4 located at Los Alamos National Laboratory. DARHT Axis-1 is a linear induction accelerator that utilizes ferrite-loaded, non-resonant magnetic induction cavities to inductively couple power into a 100-ns-long, ~1.7 kA relativistic electron bunch to accelerate the charged particles to 19.8 MeV. This single-pulsed accelerator has been operational since 1999, and produces a single high-resolution radiograph per shot. The accelerator consists of a 4-MV injector [18, 19] composed of a single Blumlein and a

graded transmission line, 64 ferrite induction cells distributed into 8 cell blocks, and the WDM experimental region shown in figure 2.5 [20] that will be explained briefly.

The diode region (fig. 2.5) is where the initial electron beam is generated from a velvet cathode [17, 21]. Ordinary velvet is used for the cathode surface due to its low threshold for electron emission (~30 kV/cm), and is typically driven by a diode voltage to produce a strong electric field (~150 kV/cm). Electrons are liberated from the surface of the cathode that leads to an electron avalanche which ionizes the hydrogen monolayers within the tufts of velvet. Only a small fraction of these electrons is extracted from the plasma sheath and accelerated across the 17.8 cm A-K gap. The current extracted through the diode is dependent on the diode voltage, diameter of the cathode, and A-K gap [22]. The electrons accelerated through the 4 MV diode are transported into the induction accelerator.

The induction accelerator consists of 8 cell blocks with 8 accelerating cells each for a total of 64 accelerating cells. Each induction cell operates at ~250 kV/cell, and contains 11 oil-insulated ferrite cores, an acceleration gap, a solenoid magnet and dipole pair to transport the electron bunch [23]. There were concerns for high-voltage breakdown when designing the cells, thus the acceleration gap was made to have a minimum width of 19 mm. The bore of the cell is approximately 146 mm to limit the transverse impedance which directly contributes to the growth rate of the beam breakup (BBU) instability [24], and to provide enough room for the solenoid magnet with reduced costs. The growth in the BBU instability depends on the cell transverse impedance, beam current, and number of acceleration gaps. An offset electron beam interacting with the transverse mode of the cell cavity induces an RF oscillation in the beam envelope that leads to degradation in the time-integrated beam spot size. Degradation in the beam will lead to increased radiographic spot size and decrease the quality of the radiograph.

The electrons accelerate to 19.8 MeV after transport through the induction accelerator, and then finally focus onto a 1-mm-thick Ta X-ray conversion target. The source spot for the Bremsstrahlung production is < 1 mm in diameter (50% MTF). There are beam position monitors (BPMs) that are used throughout the accelerator to align the beam, measure current, and minimize instabilities.

Figure 2.4: Aerial view of the DARHT Facility at Los Alamos National Laboratory.

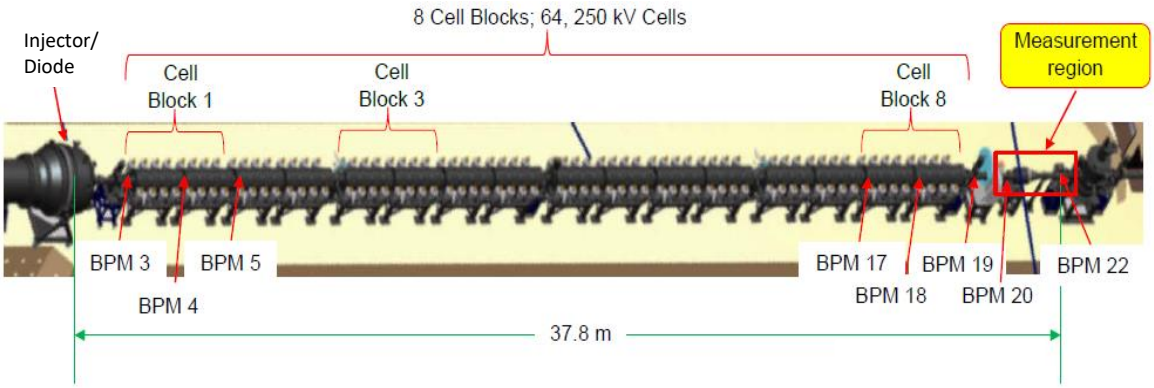

Figure 2.5: Accelerator layout of DARHT Axis-1 showing the injector, acceleration, and WDM measurement region. This excludes the downstream transport to the radiographic region.

The BPMs are discussed more thoroughly in Section 3.1.

2.2.3 The Impact of WDM on Radiographic Spot Size

The DARHT radiographic mission is to reduce the source spot size, and therefore increase radiographic quality. However, WDM produced at the targets will have unfavorable effects on the electron pulse. It should be noted that WDM is produced near the onset of the hydrodynamic disassembly time of the range-thin foils, but the 100-ns-long electron beam still deposits energy into the targets and the resulting plasma. The energy deposition during the electron pulse is dynamic, and becomes more complex with the formation of warm dense plasma. The effect of WDM on radiographic spot size is not well known, and leaves great motivation for this research. Ions generated at the target can neutralize the space charge of the beam as n_i approaches n_e, but density gradients complicate the problem. The production and transition into the warm dense phase and subsequent expansion must be understood to optimize the radiographic capability.

2.3 Heating with Relativistic Electrons

2.3.1 Collisional Stopping Power

Electrons lose their energy through collisions with matter. Electrons lose energy by collisional and radiative stopping powers (dE/dx) which are dependent on material and entrance energy; these can be found in the ESTAR database from NIST [25]. The energy deposited in DARHT target foils is calculated using the collisional stopping power since the radiative energy losses are carried away in the form of Bremsstrahlung radiation. The collisional heating process involves the relativistic electrons interacting with the material lattice, and stripping electrons from the atoms.

The relativistic electrons are near the minimum of the collisional stopping power curve at 19.8 MeV for all materials which is shown in figure 2.6, and thus the coupling of the relativistic electrons and the target is not optimized for thin foils. This inefficiency in energy transfer is true for all materials used, but cannot be avoided since high-energy Bremsstrahlung radiation is needed to penetrate dense hydrotests. Typically, less than 1% of the available particle beam energy deposits into 100-μm-thick foils.

However, it is unfavorable to increase the thickness of the targets for WDM experiments because the electron energy deposits linearly with thickness. Increasing the target's thickness will result in the increased production of Bremsstrahlung radiation that will scatter into our diagnostics, and reduce S/N ratios. It will also increase debris production, and prolong isochoric heating. In figure 2.7 (a), the current of the electron beam (shot 25916) is integrated to quantify the deposited charge onto the target foils. For example, the deposited charge over 100 ns for a 1.7 kA beam is ~130 μC. As the electron energy deposits through collisional stopping power, the foils will experience phase changes through melting, evaporation, and ionization if r < 2 mm as shown by figure 2.7 (b) for copper.

The approximate energy deposited, $\Delta E(t)$, into the target is estimated by equation 2.3. For copper the collisional stopping power, dE/dx, is 1.513 MeV-cm^2/g for a 20 MeV electron beam.

$$\Delta E(t) = q(t)\frac{dE}{dx}\rho_o \Delta z = \frac{q(t)\frac{dE}{dx}m}{\pi r^2}, \qquad \text{Equation 2.3}$$

where Δz is the foil thickness, $q(t)$ is the time dependent electron charge at the target, r is the radius of the beam, and m is the heated mass.

The energy required to melt, vaporize, or ionize the target material is estimated by equation 2.4.

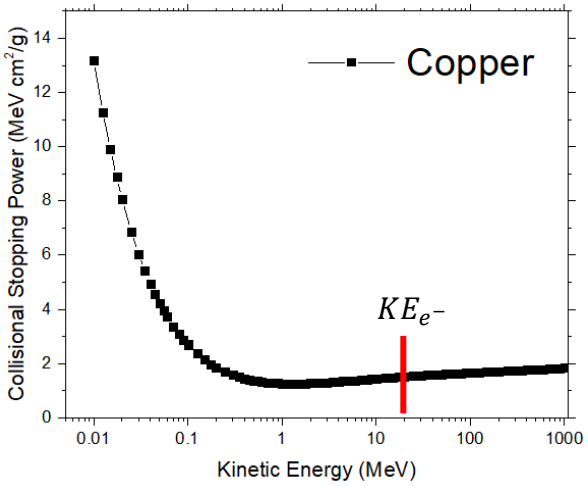

Figure 2.6: Collisional stopping curve for electrons through copper.

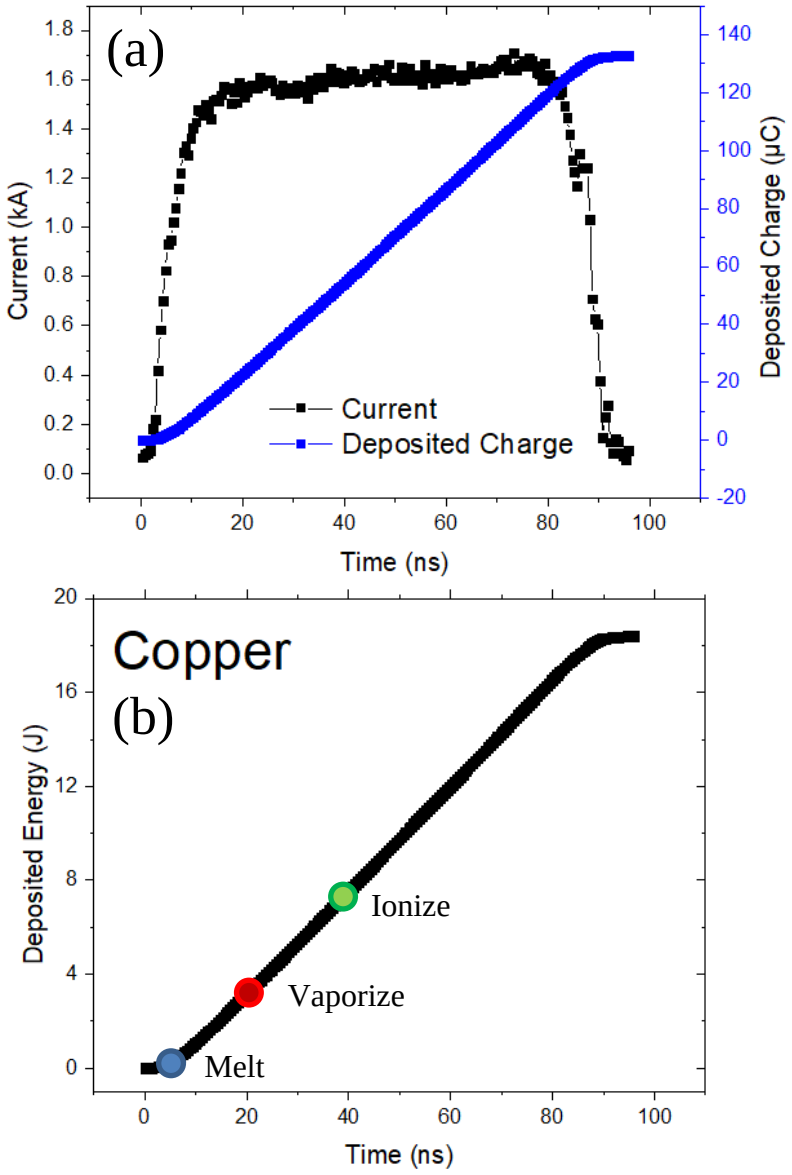

Figure 2.7: (a) The incident electron current (black) and the charge (blue) on target foils. Shown is shot number 25916. (b) The deposited energy and heating profile for 100-μm-thick copper assuming r = 0.5 mm.

$$E = Lm\,, \qquad \text{Equation 2.4}$$

where L is the latent heat of fusion or vaporization of the material [26].

Consider a 100-μm-thick foil of copper with latent heat of fusion of ~13.1 kJ/mol, latent heat of vaporization of ~300 kJ/mol, and first ionization energy of ~744 kJ/mol [27]. It would take approximately 0.13 J of deposited energy in ~4 ns to melt the copper foil, and 3 J to vaporize the copper foil in ~20 ns as indicated by figure 2.7 (b). Furthermore, it would take a deposited energy of 7.5 J to ionize the copper target in ~41 ns assuming a spot size of ~1 mm. It should be reiterated that >99% of the available particle beam energy (~2.5 kJ) passes through the foil. This is due to the range of the 20 MeV electrons in copper (1.17 cm), which is >100x the thickness of this foil. The purpose of using thin foils is to minimize Bremsstrahlung production, optimize isochoric heating, and to minimize target debris production.

2.3.2 Isochoric Heating

Isochoric heating, a constant volume process, is necessary for production of large, homogenous samples of WDM. DARHT Axis-1 provides a method to heat range-thin foils in a two-stage process with a monochromatic 20 MeV, multi-kA bunch of electrons. The isochoric heating method used with DARHT is a slower heating method compared to the isochoric photon heating method used in laser shock-compression experiments [20].

As mentioned, the heating occurs in two stages. The first stage is early in the electron pulse before the material hydrodynamically disassembles, $t < t_{hydro}$. This first stage is considered isochoric since the material does not expand considerably, and >50% of solid density of the material remains constant. As it will be shown, the hydrodynamic disassembly time is the point when pressure release occurs in the foil as measured by the PDV diagnostic. Before this disassembly occurs, the foil experiences pressure and temperature buildup during the electron pulse. As the foil experiences phase changes of melting, vaporization, and ionization, the material disassembles and the heating is no longer isochoric. However, it will be shown that measurements are still taken after hydrodynamic disassembly while the electron pulse deposits energy into the resulting plasma plume.

CHAPTER THREE – DATA ACQUISITION

3.1 Beam Distribution and Current Density Measurements

3.1.1 Beam Position Monitors

Beam position monitors (BPMs), used throughout the length of DARHT Axis-1, are non-invasive diagnostics commonly found in linear accelerators, cyclotrons, and synchrotrons [28]. Invasive diagnostics used in Axis-1 include intercepting foils and Cerenkov emitters for measuring beam current density profiles, or magnetic spectrometers for measuring the beam kinetic energy and longitudinal phase space. BPMs are located at the exit of the injector, after every four cells in the accelerator, and in the downstream transport section of Axis-1 [17]. The BPMs measure beam position, current, and RF oscillations on the beam, which provides scientists the necessary information to properly tune and align the accelerator for optimal transport. BBU and centroid oscillations can reduce the beam quality and lead to emittance growth that degrades the radiographic spot size.

BPMs are an array of B-dots, or inductors, which measure the current induced by the passing electron pulse in the B-dot. The BPMs are calibrated with known offsets for each B-dot relative to the mechanical and magnetic centerlines of the accelerator. The measured current can vary spatially and temporally depending on the beam alignment and distribution. We implement the BPM21 current profile measurement, shot 25916, in HELIOS-CR and LASNEX. This BPM measurement gives a characteristic current profile of Axis-1 as shown in figure 2.7 (a).

3.1.2 Optical Transition Radiation

An optical transition radiation (OTR) measurement provides the current density, $J(x, y)$, of the electron beam in the near-field (Fresnel zone) shown in figure 3.1 [12]. As a charged particle approaches and moves across a boundary of two different media with different dielectric constants, a perturbation in the particles associated electromagnetic field occurs [29]. This perturbation, or reorganizing of the electromagnetic field as the particle transitions to a new medium, releases transition radiation. An ICCD camera captures this near-field visible transition radiation measurement, and figure 3.1 illustrates an example

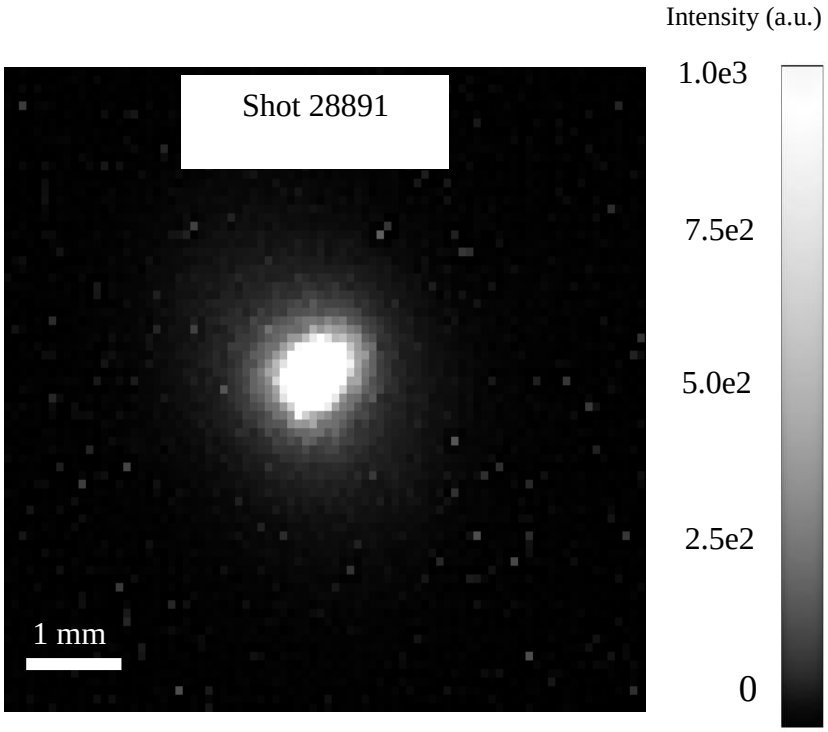

Figure 3.1: (a) A near-field OTR measurement for shot 28891 with appropriate scale length shown.

for shot 28891 (4 mil Al). The ICCD camera, mounted upstream of the vacuum vessel, captures the forward-scattered OTR on the back side of the foil with a 20º offset. The measurement is taken 20 ns after the beginning of the electron pulse, ~30 ns before plasma formation.

An extracted gaussian profile from the OTR measurement yields the approximate spot size of the focused electron beam. For the copper and titanium foil experiments described in section 4.1.1, the gaussian profile yields a spot size of ~2 mm FWHM. A spot size of ~1 mm FWHM is measured for the Al, Ni, and C foils outlined in section 4.1.2. The hydrodynamic codes utilize these spot size values to replicate the experiments as best as possible.

3.2 Foil Motion Measurements with PDV

The two techniques typically used in the plasma physics and shock physics communities that measure velocity on shock-compressed materials include a velocity interferometer system for any reflector (VISAR) [30], and photonic Doppler velocimetry (PDV) [31]. The hydrodynamic motion of the foils heated by an intense electron beam using PDV will be discussed. This worked is largely based off of the recently published work on copper [32].

The PDV probe, implemented on Axis-1, instantaneously measures foil motion, displacement at the edge, and inferred plasma pressure in the elastic limit. The probe, a single collimated laser (λ = 1550 nm), is directed at the foil surface with a working distance of ~36 cm. Figure 3.2 best illustrates the process of heating the target foil, and measuring the hydrodynamic motion with the PDV probe. The probe, offset by 20º relative to the foil surface, avoids any interactions with the electron beam. Due to this offset, it measures the motion of the foil with a factor of $v_z \cos(20^\circ)$. Since the probe wavelength is on the order of the surface roughness (~2 μm), it measures the nonspecular backscattering from the foil. It should be noted that the probe only measures along the probe axis, and does not provide complete information on the spherical plume expansion. However, multiple PDV probes positioned at various angular offsets would yield plume expansion measurements.

In figure 3.2, an optical fiber transports the laser light to a probe directed at the foil surface. This laser light illuminates the foil surface and reflects back into the same probe

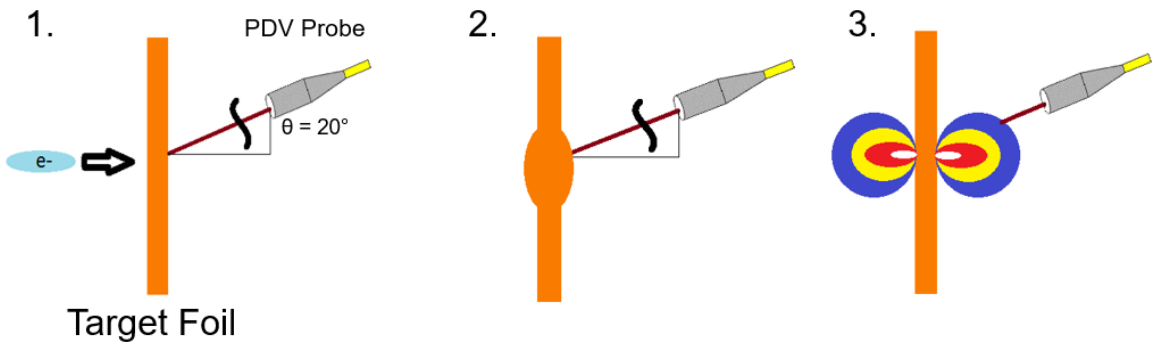

Figure 3.2: Illustration for target heating and PDV measurement.

[fig. 3.2 (1)]. As the surface expands during energy deposition [fig. 3.2 (2-3)], the reflected light becomes Doppler-shifted with some Doppler-shifted frequency, f_D. This Doppler-shifted light interferes with the original laser light with a non-Doppler-shifted frequency, f_o. The operating wavelength of the laser, 1550 nm, corresponds to a frequency of $f_o = 193\,THz$. The two sinusoidal wave forms of different frequencies generate a beat frequency, $f_{beat} = f_D - f_o$. The wave forms travel to a detector and digitizer with a bandwidth high enough to measure f_{beat}. For example, a velocity of 1000 m/s corresponds to a beat frequency of ~1.29 GHz, and it will be shown that our PDV measurements sometime exceed 4 km/s. Thus, the detector system must have a total bandwidth exceeding the multi-GHz range.

Figure 3.3 (a) illustrates the measured voltage response with the detector system for shot 25901, a 200-μm-thick Cu foil, with a 250 ns snapshot and 13.5 μs window in the inset. The voltage response is the beat wave calculated from the interference of the two frequencies mentioned above. Figure 3.3 (a) shows a large voltage response at $t \approx 20$ ns to ~225 mV. The response exhibits the instantaneous measurement at the beginning of energy deposition and foil heating.

The signal noise before the initial response is $\pm$25 mV yielding a S/N ratio of 9 at $t \approx 20$ ns. This S/N ratio decays during the electron pulse and as the foil hydrodynamically disassembles. The foil velocity during the pulse is calculated from the measured beat frequency and the original probe wavelength.

$$v(t) = \frac{1}{2} f_{beat} \lambda_o \,, \qquad \text{Equation 3.1}$$

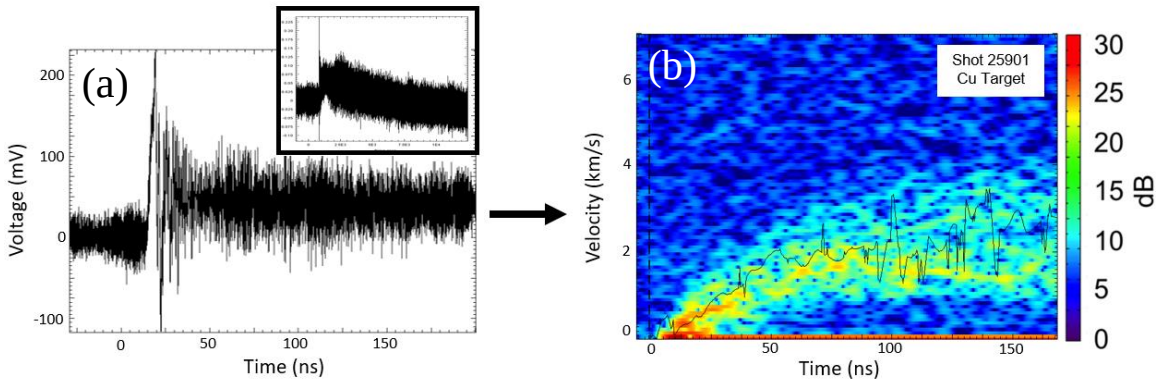

Figure 3.3: (a) Beat wave response measured with the PDV diagnostic. (b) Velocity spectrogram calculated from the voltage response.

where λ_o is the probe reference wavelength of 1550 nm. Figure 3.3 (b) shows the calculated velocity spectrogram from the voltage response for shot 25901. A velocity spread occurs later in time due to the probe penetrating an expanding Cu plume with fast and slow particles (ejecta) crossing the probe path.

The spectrogram yields the averaged velocity profile by selecting a region-of-interest within a signal threshold of 10 dB around the velocity spread measured from the beat response. This averaged velocity profile is overlaid on the spectrogram in figure 3.3 (b). Integrating the averaged velocity profile yields the averaged displacement of the foil at the edge shown in equation 3.2.

$$< \delta z >= z_o + \int < v > dt \,, \qquad \text{Equation 3.2}$$

The foil is initially static during the isochoric heating stage of the pulse. As the foil hydrodynamically disassembles, and the pressure in the elastic limit is calculated by

$$P_E(t) = \frac{1}{2} C_0 v(t) \rho(t) \,, \qquad \text{Equation 3.3}$$

where C_0 is the sound speed of the material, and $\rho(t)$ is the calculated density along the probe path. This density stems from the expanded volume $V(t) = V_o + 2A\delta z$ and the heated mass of the probed material, where A is the interrogated area of the probe, and V_o is the initial probed volume. The calculation of the elastic pressure provides an approximation since we only consider the expanded volume along the probe's axis. Extracting the pressure in the elastic limit before plastic deformation is applied to the foil PDV measurements in

Chapter 4 for Cu, Ti, Ni, Al, and C. The resulting pressure profiles yield the hydrodynamic disassembly times, or when the foils experience pressure release during energy deposition.

3.3 Numerical Simulations

3.3.1 The HELIOS-CR Code

The numerical code used for the majority of this project is the 1-D radiation-magneto-hydrodynamic software HELIOS-CR [33]. This code primarily exists in the inertial confinement fusion community for laser-produced plasma and z-pinch plasma simulation [34, 35]. However, a new capability that simulates electron energy deposition has been implemented and allows simulation of WDM experiments.

HELIOS-CR allows user specification of experimental geometries in the initial simulation setup. The user specifies a planar, spherical, or cylindrical geometry that best replicates their experiment. The planar geometry suits the WDM experiments and simulates the foil targets. The simulated target is specified for thickness, material properties, the EOS models, and the optical properties. Initiated material properties include density, starting temperature, and thermal conductivity. The Spitzer model substitutes for the material thermal conductivity. EOS and optical tables used in the WDM simulations are pulled from PROPACEOS tables [36], but the HELIOS program can utilize other EOS models such as SESAME [37].

HELIOS-CR utilizes Lagrangian methods that solve conservation equations. The simulated geometry must be broken into discrete zones for computational purposes, often referred to as meshing the structure. The Lagrangian method involves the mesh moving with the fluid as it either expands or contracts during simulation which makes solving the complex hydrodynamic problems simpler. In the WDM experiments, a user-specified number of zones determines the resolution of the meshing structure. Typically, the higher number of zones correspond to a higher degree of accuracy, but costs increased computational time. For WDM simulations, a 1 zone/μm mesh meets accuracy and computational time requirements (i.e. a 100 μm foil would be broken into 100 zones).

It is assumed for simplification purposes that the energy transport in the plasma exhibits one-temperature ($T_e = T_i$) behavior, and that the electrons and the ions assume

Maxwellian distributions. Moreover, the user defines an input temperature for when materials initiate hydrodynamic motion. Initially, the materials are solid and static, and hydrodynamic motion occurs once it reaches the user defined temperature during energy deposition. Hydrodynamic motion corresponds with an expansion or contraction of the material, and the melting temperature of the material substitutes for this threshold. For example, the hydrodynamic motion threshold for copper would be its melting temperature of 1356 K, or 0.12 eV. Furthermore, the resulting plasma during energy deposition assumes local thermodynamic equilibrium (LTE). HELIOS-CR can model non-LTE kinetics of plasmas, but become quite complex and fall outside of this project's scope.

3.3.2 The HELIOS-CR Electron Beam Capability

As mentioned previously, the electron energy deposition capability has been added in HELIOS-CR. Electron transport follows the Monte Carlo approach, and the incident boundary, electron energy, and the beam power require user specification. Particle accounting and transport occurs at every time step, ensuring a spatially smooth particle deposition. The code accounts for electronic stopping powers that determine how much energy is transferred to the material as the beam travels through each volumetric element. The code automatically tabulates the stopping energy curves for each specified element from the ESTAR database from NIST [25].

For comparative purposes, the simulation specifications ensured replication of the WDM experiments to a feasible extent. Figure 3.4 shows the power density ($\frac{TW}{cm^2}$) profile of the simulated electron beam used for the copper and titanium HELIOS-CR simulations. This power density profile assumes a spot size of 2 mm. The simulated electrons are monoenergetic at 19.8 MeV, and the current profile is provided by the measurement at BPM21 for shot 25916. The copper and titanium simulations utilized a current with flat top at approximately 1.7 kA. Similar beam parameters are utilized for Al, C, and Ni foils, but with a flat top at approximately 1.44 kA. The HELIOS-CR code provides simulated values for density, temperature, velocity of the foil, and the pressure. These simulated hydrodynamic values are compared to the experiments for benchmarking purposes.

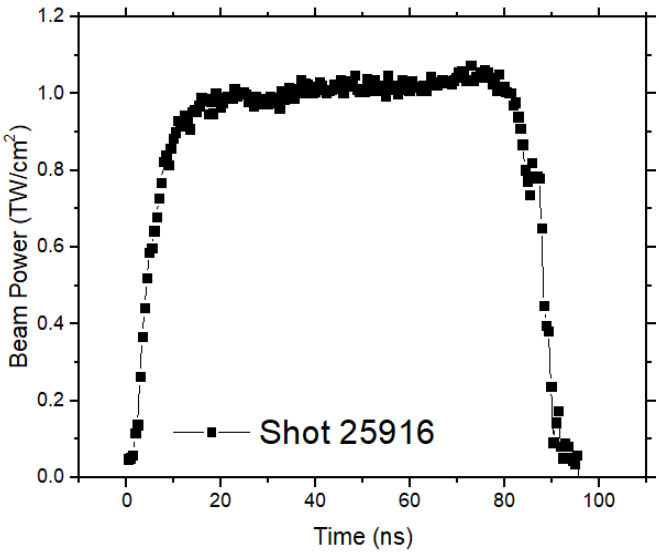

Figure 3.4: Beam power input for simulated copper and titanium foils in HELIOS-CR.

3.3.3 The LASNEX Code

LASNEX, a 2-D Lagrangian radiation-hydrodynamics code, explores the physical processes of inertial confinement fusion and aids in target design [38]. It is used to benchmark a wide variety of heating methods such as laser, electron, and ion beam experiments. The LASNEX simulation evolves in time a 2-dimensional axially-symmetric plasma generated by an electron beam heated geometry in WDM simulations [32]. The code solves the Navier-Stokes equations with specified artificial viscosity and electron thermal conduction, including multigroup radiation transport. LASNEX utilizes the collisional stopping power curves for electrons and ionization cross sections to accurately model the experiments, and utilizes SESAME EOS tables. The simulated current density in the 2-D hydrocode mimics the measured OTR response for each set of experiments. Additionally, user specification of the current pulse and the energy deposition rate accurately models the foil experiments. This 2-D hydrodynamic code estimates the hydrodynamic quantities of electron temperature, density, velocity of the leading edge of the foil, and pressure within the foil utilizing the SESAME EOS tables. This allows direct comparison of the advanced LASNEX simulations to the experimental PDV data, and the 1-D hydrocode, HELIOS-CR.

CHAPTER FOUR – RESULTS AND DISCUSSION

4.1 Photonic Doppler Velocimetry Results

4.1.1 The Role of Foil Thickness on t_{hydro}

The role of foil thickness on hydrodynamic disassembly time, t_{hydro}, is explored with the PDV diagnostic. Copper and titanium foils of 50, 100, and 200 μm thickness undergo energy deposition with the characteristic DARHT pulse of 80 ns FWHM, KE of 19.8 MeV, current of 1.7 kA, and beam spot size of 2 mm on each foil. The role of foil thickness on t_{hydro} is achieved by holding beam parameters constant from shot to shot. It has been hypothesized that the hydrodynamic disassembly time for a rectangular two-dimensional foil is found by equation 4.1.

$$t_{hydro} = \frac{\Delta z}{2C_0}, \qquad \text{Equation 4.1}$$

where Δz is the foil thickness, and C_0 is the sound velocity at ambient pressure. This equation assumes expansion on both sides of the target. The sound velocities at ambient pressure for copper and titanium are 3.93 km/s and 4.94 km/s. These values are found from Hugoniot data tables [39]. Equation 4.1 states that the hydrodynamic disassembly time scales linearly with foil thickness, and these set of experiments were conducted to study this approximation.

Figure 4.1 (a-f) summarizes the PDV results made for copper foils of varying thickness (2 mil ≈ 50 μm) where $t = 0$ is the onset of the electron pulse. Figure 4.1 (a), (b), and (c) illustrate the spectrograms obtained from the beat wave response for 50, 100, and 200-μm-thick copper foils during energy deposition, respectively. The spectrograms exhibit no presence of a shock. Figure 4.1 (d) compares the experimental average foil velocity, (e) compares the average foil displacement at the edge, and (f) compares the average elastic pressure of each copper foil.

The average particle velocity exhibits a linear ramp in the first ~30 ns, and then begins to flatten after disassembly for each foil. This reduction in acceleration coincides with pressure release and the hydrodynamic disassembly of the foil. The achieved particle velocity increases as a function of foil thickness as shown by figure 4.1 (d).

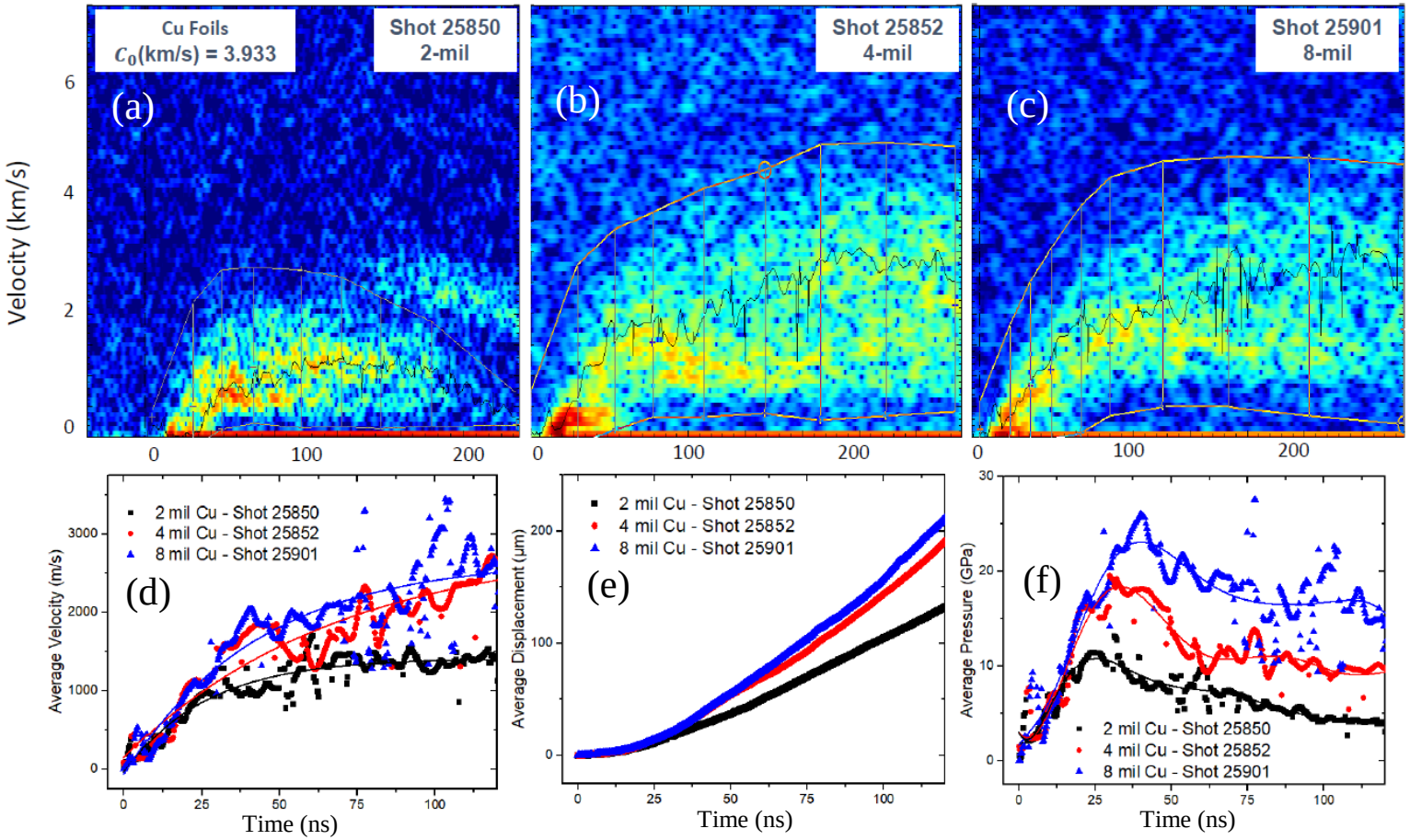

Figure 4.1: Experimental measurements of copper foils with the PDV probe. (a-c) Spectrograms for 50, 100, and 200-μm-thick Cu foils, (d) average particle velocity, (e) average foil displacement at the edge, and (f) average elastic pressure in the foil.

As a result, the foil displacement at the edge increases with foil thickness as indicated by figure 4.1 (e). Thicker foils achieve higher inferred pressures, and later hydrodynamic disassembly times indicated by 4.1 (f). The hydrodynamic disassembly time is defined as the point where the foils experience a pressure release, or the peaks in the pressure profiles. Table 4.1 summarizes the hydrodynamic values obtained from the PDV data for copper.

In table 4.1, the hydrodynamic disassembly time, t_{hydro}, increases from ~25 ns for 50-μm-thick Cu to ~40 ns for 200-μm-thick Cu. The heated mass increases with foil thickness, and leads to increased energy deposition and later values of t_{hydro}.The heating process is isochoric until the hydrodynamic disassembly time since >50% of the density remains constant until this point. As indicated in table 4.1, the average particle velocity, $\langle v \rangle$, increases from 0.9 km/s for 50-μm-thick Cu to 2.0 km/s for 200-μm-thick Cu at t_{hydro}, more than a 2x increase. The average displacement of the foil edge, $\langle \delta z \rangle$ (Eq. 3.2), at t_{hydro} increases from 14 μm for the thinnest foil to 37 μm for the thickest foil, and results from increased particle velocity as Δz increases. Calculated pressures in the elastic limit, $\langle P \rangle$ (Eq. 3.3), at t_{hydro} of each foil are 11, 18, and 24 GPa for the 50, 100, and 200-μm-thick Cu foils, respectively. The 24 GPa pressure achieved in the 200-μm-thick foil at $t = 40\ ns$ is near the solid-density Fermi pressure, 33 GPa [40]. As the thickness increases, the energy deposited in the material from electronic collisions is estimated by equation 4.2 [10].

$$\Delta E_{dep} = q \frac{dE}{dx} \rho_o \Delta z\ , \qquad \text{Equation 4.2}$$

Table 4.1: Summary of hydrodynamic values for copper foils.

Foil Thickness (μm)	t_{hydro} (ns)	$\langle v \rangle$ @ t_{hydro} (km/s)	$\langle \delta z \rangle$ @ t_{hydro} (μm)	$\langle P \rangle$ @ t_{hydro} (GPa)
50	25	0.9	14	11
100	31	1.4	21	18
200	40	2.0	37	24

Thicker samples of an identical material will see more electronic collisions and as a result an increase in deposited energy and heating time. This will lead to later hydrodynamic disassembly times, increased foil pressures, higher particle velocities, and displacements.

Titanium foils of varying thickness exhibit similar behavior compared to copper. Hydrodynamic values for titanium foils (50, 100, and 200 μm) are summarized in table 4.2. The data in table 4.2 indicates the disassembly time for 50 and 100 μm Ti foils are approximately equal at 25 ns and 26 ns, respectively. The hydrodynamic disassembly time increases, however, for the 200 μm foil to 33 ns. The other hydrodynamic values at t_{hydro} differ greatly as a function of Δz indicated by the average velocity, displacement of the foil, and inferred pressure.

The experimental measurements do not follow the linear relationship exhibited by equation 4.1. Figure 4.2 illustrates the hydrodynamic disassembly time as a function of material thickness, where Ti data clearly shows a nonlinear relationship. Copper may exhibit the linear relationship between hydrodynamic disassembly time and material thickness, but similar experiments with thicker foils need to be studied. This would involve repeating the experiments with foils of 500, or 1000 μm thickness. However, HELIOS-CR indicates a linear relationship between t_{hydro} and Δz as outlined in Section 4.2.

The PDV diagnostic yields an additional approximation, the electron and ion temperatures after foil disassembly. The electron temperature, T_e, is calculated from the average velocity, or sound speed, from the PDV measurements indicated in figure 4.1 (d). The particle velocities approach the sound speed after the hydrodynamic disassembly of the foil. If we assume that the measured velocity from the PDV data mimics the ion sound velocity after disassembly, equation 4.3 yields the electron temperature [41].

$$T_e \approx \frac{C_s^2 m_i}{\gamma Z k_B}, \qquad \text{Equation 4.3}$$

where m_i is the mass of the ion, γ is the adiabatic index or isentropic expansion factor which is 5/3 for a monoatomic metallic plasma, Z is the charge state of the plasma (assumed to be 1), and k_B is the Boltzmann constant.

We assume the velocity spread in the PDV data after disassembly mimics the

Table 4.2: Summary of hydrodynamic values for titanium foils.

Foil Thickness (μm)	t_{hydro} (ns)	<v> @ t_{hydro} (km/s)	<δz> @ t_{hydro} (μm)	<P> @ t_{hydro} (GPa)
50	25	1.5	14	12
100	26	2.6	44	17
200	33	2.8	55	21

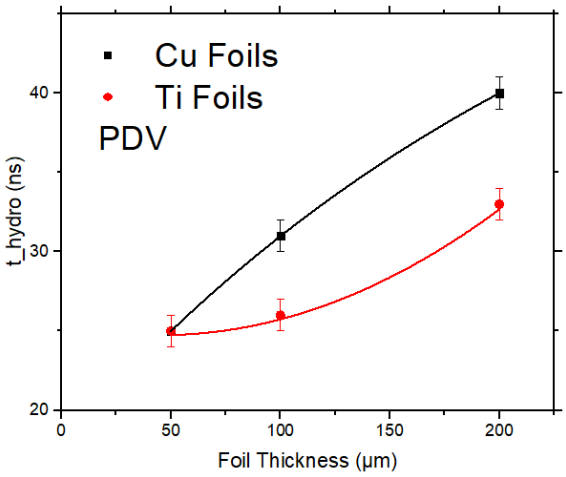

Figure 4.2: Hydrodynamic disassembly time as a function of foil thickness for Cu and Ti.

plasma thermal ion distribution, so an approximation of the ion temperature is found. The spread in the PDV data, as described previously, occurs from the range of fast and slow particles (ejecta) the PDV probe interrogates. Equation 4.4 yields an approximation in the ion temperature.

$$T_i \approx \frac{v_{T_i}^2 m_i}{k_B}, \qquad \text{Equation 4.4}$$

where v_i is the velocity spread directly in PDV measurements.

Figure 4.3 (a) and (b) show the approximate electron and ion temperature of the copper PDV measurements. Figure 4.3 (a) shows the electron temperature increases as a function of foil thickness. The approximate electron temperature after disassembly is ~0.2-0.3 eV from 25-120 ns for the 50-μm-thick Cu foil in shot 25850. T_e reaches ~0.5 eV from 30-75 ns for 100-μm-thick Cu foil in shot 25852, and then quickly increases to ~1.2 eV at 120 ns. Electron temperatures range from 0.7 eV at 45 ns to ~1.5 eV at 120 ns for the thickest Cu foil of 200 μm in shot 25901. Fig. 4.3 (b) shows the ion temperatures calculated from the PDV data. There is no clear correlation seen in the ion temperature profiles for the Cu foils throughout the duration of the electron pulse. However, these approximations exhibit the two-temperature assumption, $T_e \neq T_i$, that is expected in WDM experiements.

The approximation in electron and ion temperatures from the PDV measurements require benchmarking with other diagnostics.

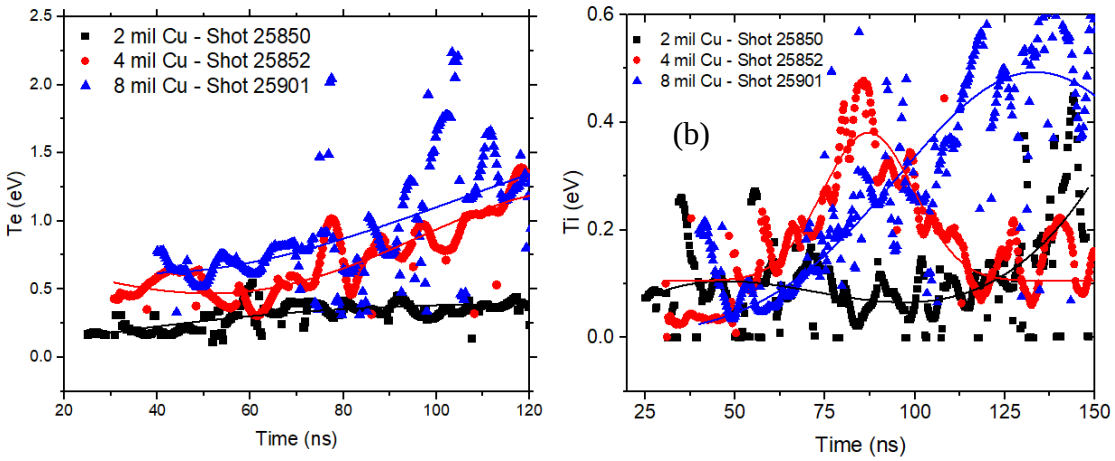

Figure 4.3: Calculated Cu (a) electron and (b) ion temperatures from PDV measurements.

These diagnostics include UV and X-ray spectrocopy diagnostics, which yield time-resolved measurements of electron and ion temperatures, and charge state. Interferometry implemented on Axis-1 would yield electron density measurements.

4.1.2 The Role of Target Material on t_{hydro}

The role of foil material on foil hydrodynamic behavior is explored. Metallic foils of Al 1100 and Ni, as well as a nonmetallic foil of pyrolytic carbon are heated with a 100-ns-long relativistic electron bunch with 1.44 kA of beam current, and a spot size of ~1 mm FWHM. The 1.44 kA of beam current corresponds to ~113 μC of deposited charge on the Al, Ni, and C foils. The thickness of the foils is held constant at 100 μm, as well as the beam parameters from shot to shot to study the role of the target material on the hydrodynamic behavior. The PDV diagnostic obtains the hydrodynamic quantities of particle velocity, foil displacement, pressure in the elastic limit, and the hydrodynamic disassembly time.

It is important to quantify the deposited energy into each foil using equation 4.2. The deposited energy is based off of the electronic collisional stopping power in each material at ~20 MeV, the solid density of the material, and the deposited charge. As stated previously, the beam current of 1.44 kA corresponds to ~113 μC of charge, while the 1.7 kA beam current used for the Cu and Ti foils provided ~130 μC of deposited charge. We cannot directly compare the Ni, Al, and C data to the Cu and Ti data since the total charge, spot size and envelope were different in the two experiments. However, two experiments with different beam parameters offers the ability to benchmark more scenarios in HELIOS-CR. Furthermore, no conclusions can be drawn yet of these experiments, but provide further benchmarking capability for the hydrocodes.

Table 4.3 lists the deposited energy in each foil based off of the stopping power, deposited charge, and material properties for Al, Ni, and C. These values are based off of a beam current of 1.44 kA, and spot size of ~1 mm. Table 4.4 lists the deposited energy for Cu and Ti foils with a beam current of 1.7 kA, and a spot size of ~2 mm. These tables illustrate that only a small portion of the available beam energy (multi-kJ) deposits into each foil. A 100-ns-long, 1.7 kA beam at 19.8 MeV will have a total available energy of

Table 4.3: Values of stopping power, deposited charge, and deposited energy for 100 μm foils of C, Al, and Ni. Assumes a beam spot size of 1 mm.

Element	ρ_0 (g/cm^3)	$\left(\frac{dE}{dx}\right)_{col}$ @ 20 MeV (MeV/cm)	E_{dep} (J)
Pyrolytic C	2.2	3.97	4.49
Al 1100	2.7	4.60	5.20
Ni	8.91	14.1	15.9

Table 4.4: Values of stopping power, deposited charge, and deposited energy for 100 μm foils of Cu and Ti. Assumes a beam spot size of 2 mm.

Element	ρ_0 (g/cm^3)	$\left(\frac{dE}{dx}\right)_{col}$ @ 20 MeV (MeV/cm)	E_{dep} (J)
Ti	4.51	7.14	10.0
Cu	8.96	13.6	19.0

~3.4 kJ, which is roughly two orders of magnitude greater than the deposited amounts. The estimated deposited energy into pyrolytic carbon, similar to Al, is approximately 5 J, and about three times less than the estimated energy in Ni foils at 15.9 J. The energy deposited and material properties (phase diagram) play a role in the hydrodynamic behavior of the foils.

We apply the same PDV analysis to Al, C, and Ni foils to obtain hydrodynamic values. These include the average particle velocity, foil displacement at the edge, and inferred pressure in the elastic limit. Figure 4.4 (a-b) illustrates the inferred pressures of each foil material at 100 μm thickness. Recall the separate beam parameters for each experiment.

It is clear that the material has a significant effect on the hydrodynamic behavior, especially the hydrodynamic disassembly time and the inferred pressure as exhibited in figure 4.4 (a). Shot 28901, a Ni foil, achieves an inferred pressure of ~31 GPa at t_{hydro} of ~19 ns, while the carbon target reaches an inferred pressure of ~3.6 GPa at t_{hydro} ~42 ns. The carbon hydrodynamic disassembly occurs much later compared to foils of Ni or Al, and results from multiple factors. The optical and specific latent heat properties, deposited energy, and sound speed of the material will play a role in the hydrodynamic behavior.

Table 4.5 lists the sound speed, S/N ratio from each beat wave response, hydrodynamic disassembly time, and the inferred plasma pressure at t_{hydro} to summarize the hydrodynamic results based on material effect. These values, as well as the values obtained for the thickness experiments, are compared to the LASNEX and HELIOS-CR simulations in section 4.2.

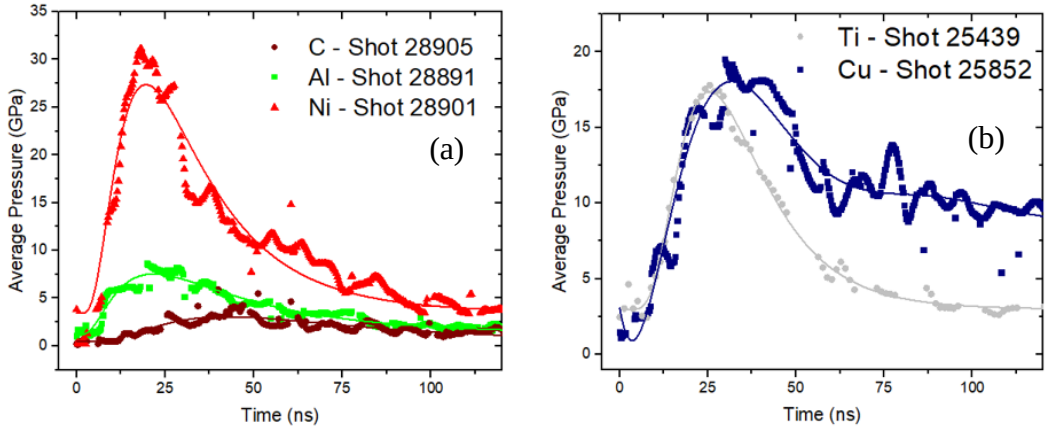

Figure 4.4: Inferred plasma pressures for targets of (a) Al, Ni, C, and (b) Ti, and Cu. All foils are 100-µm-thick.

Table 4.5: Summary of hydrodynamic values for Al, Ni, C, Cu, and Ti foils. Included are the S/N ratios from the beat waves. *Not at ambient pressure.

Element	C_0 (km/s)	V Response S/N	t_{hydro} (ns)	<P> @ t_{hydro} (GPa)
Pyrolytic C	5.11*	2.5	42	3.6
Al 1100	5.23	19	21	8.0
Ni	4.52	2.9	19	30.5
Ti	4.94	1.8	26	17.6
Cu	3.93	14	31	18.3

4.2 HELIOS-CR Results

4.2.1 The Role of Simulated Foil Thickness on t_{hydro}

HELIOS-CR, a 1-D hydrodynamic code, simulates the WDM foils studied with the PDV diagnostic. The copper and titanium simulations are conducted with a current of 1.7 kA, and spot size of 2 mm based off of the OTR measurements in Section 3.1.2. Additionally, the Al, Ni, and C foils are simulated with a beam current at 1.44 kA, and spot size of 1 mm based off of experimental beam parameters. The code simulates the thickness effect and the material effect on t_{hydro} with these user specifications.

Figure 4.5 shows the thickness effect on the foil pressure, and hydrodynamic disassembly time for simulated copper foils with 1 ns resolution. The disassembly time, as well as the centerline pressure, increases with Δz as seen in the experiments. During the initial heating stage, $t < t_{hydro}$, the pressure builds up linearly across the foils until a point of hydrodynamic disassembly. The foils experience pressure release at t_{hydro}, and a significant drop in pressure is observed. There is a second peak present in the pressure profiles due to the electron beam depositing energy up until ~100 ns into the simulation. Thus, the foil disassembles and an increase in pressure later in time, $t > t_{hydro}$, is observed around ~100 ns. After the electron pulse, the foil pressure decays gradually as the simulated plasma expands in time and space.

Similar simulations are conducted with titanium foils of varying thickness, and a summary of the hydrodynamic values for copper and titanium are shown in table 4.6. The HELIOS-CR simulations show comparable thickness effects on the hydrodynamic motion to the PDV measurements in Section 4.1. The thinnest Cu foil, 50-μm-thick, achieves a centerline pressure of 10.6 GPa at $t_{hydro} = 21\ ns$, and increases to 24.8 GPa at $t_{hydro} = 38\ ns$ for the 200-μm-thick Cu foil. Similarly, the 50-μm-thick titanium foil reaches a centerline pressure of 7 GPa at $t_{hydro} = 24\ ns$, and the 200-μm-thick foil reaches 12.3 GPa at $t_{hydro} = 36\ ns$. The simulated hydrodynamic values show a clear thickness effect in that a later t_{hydro} and centerline pressure is achieved with increased thickness.

Figure 4.6 (a) illustrates the calculated relationship between foil thickness and the hydrodynamic disassembly time.

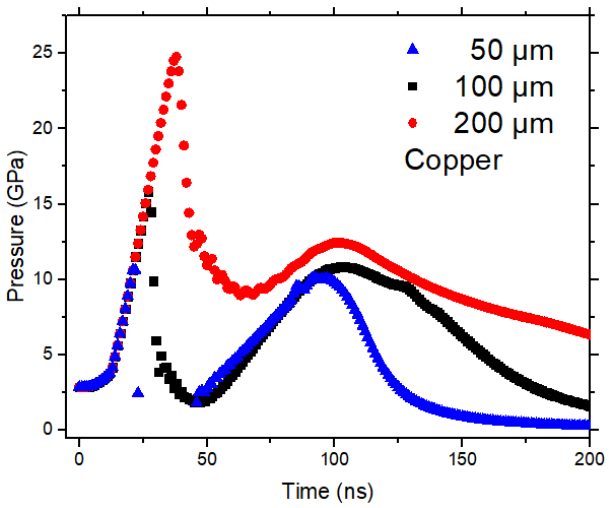

Figure 4.5: Simulated pressure profiles of 50, 100, and 200-µm-thick copper foils in HELIOS-CR. The beam current is 1.7 kA, and spot size of 2 mm.

Table 4.6: Simulated Ti and Cu hydrodynamic values in HELIOS-CR.

Element	Foil Thickness (µm)	Simulated # of Zones	t_{hydro} (ns)	<P> @ t_{hydro} (GPa)
Copper	50	50	21	10.6
	100	100	27	15.8
	200	200	38	24.8
Titanium	50	50	24	7.0
	100	100	28	8.9
	200	200	36	12.3

Unlike the experimental PDV measurements, the simulated disassembly times clearly follow a linear relationship with thickness for copper and titanium foils. The hydrodynamic disassembly times for titanium and copper are fairly consistent with each other. Additional simulations of 500 μm and 1000 μm are plotted to confirm the linear relationship described by equation 4.1. 500-μm-thick copper reaches a centerline pressure of 44 GPa at $t_{hydro} = 68\ ns$, while the 1000-μm-thick foil achieves a pressure of 67 GPa at $t_{hydro} = 107\ ns$. This result suggests that a copper foil of ~1 mm will disassemble ~10 ns after the electron pulse. In DARHT hydrotests, a 1-mm-thick Ta conversion target will also disassemble near the end of the electron pulse.

The simulated electron temperatures of the three copper foils, shown in figure 4.6 (b), are largely similar to one another. At early time, T_e increases ~linearly with time as the beam deposits energy into the foil up until the end of the pulse. The simulated temperature then decays in time after energy deposition occurs. The HELIOS-CR simulations suggest the foil thickness has little effect on the electron temperature as compared to the PDV calculations in Section 4.1. The simulated ion temperatures follow the same trends since the hydrodynamic simulations are set up to follow a one-temperature model ($T_e = T_i$). Future simulations will explore the two-temperature regime as observed in the PDV measurements.

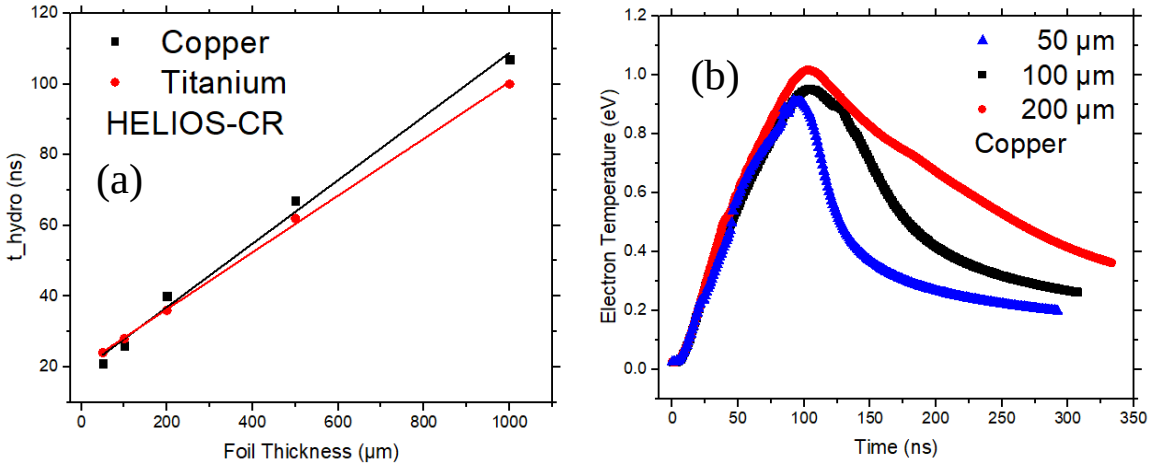

Figure 4.6: (a) Simulated relationship between the thickness and hydrodynamic disassembly time for titanium and copper foils. (b) Simulated electron temperature for copper foils

4.2.2 The Role of Simulated Target Material on t_{hydro}

The preliminary data on the material effect on t_{hydro} is simulated with HELIOS-CR. Simulated foils of Al, Ni, and C of 100 μm thickness are irradiated with a 100-ns-long relativistic electron beam with current of 1.44 kA, and spot size of 1 mm. The hydrodynamic values of centerline pressure and t_{hydro} are extracted at the point of pressure release. These simulations mainly serve to benchmark the PDV values obtained in Section 4.1.

Table 4.7 summarizes the simulated hydrodynamic values obtained for Al, Ni, and C foils. Disassembly times vary widely across the materials, comparative to the PDV measurements. Pyrolytic carbon achieves a centerline pressure of 3.6 GPa at $t_{hydro} = 42\ ns$, much later in time compared to other foils of similar thickness. Al 1100 reaches a centerline pressure of 8.0 GPa at $t_{hydro} = 21\ ns$, and Ni reaches 30.5 GPa at $t_{hydro} = 19\ ns$. A Ni foil of the same thickness achieves a pressure nearly 4x Al, or 8.5x pyrolytic carbon. This wide range of hydrodynamic values results from a multitude of factors including the density of the material, energy deposited, thermal conductivity, optical and EOS models, and latent heat properties.

Table 4.7: Summary of hydrodynamic values for simulated Al, Ni, and C foils. Each foil is 100-μm-thick

Element	t_{hydro} (ns)	<P> @ t_{hydro} (GPa)
C	42	3.6
Al	21	8.0
Ni	19	30.5

4.3 Numerical and Experimental Comparison

The purpose of this section is to benchmark the hydrodynamic codes with the experimental results. As it will be shown, the hydrodynamic codes simulate the WDM experiments with accuracy, and lay the groundwork for further experimental development. We compare the simulated hydrodynamic values to the values obtained through PDV measurements. PDV

and HELIOS-CR results are compared to LASNEX simulations for 100 and 200-μm-thick copper and titanium.

Table 4.8 (a-b) summarize the results for Cu and Ti PDV measurements, and their respective hydrodynamic simulations. It is shown in Table 4.8 (a) that HELIOS-CR simulates the warm dense foils with great accuracy. In the PDV measurement for 200-μm-thick Cu, a pressure of 24 GPa at $t_{hydro} = 40\ ns$ is achieved. HELIOS-CR, with relevant beam parameters, achieves a simulated pressure of 24.8 GPa at $t_{hydro} = 38\ ns$. The 1-D HELIOS-CR simulations agree well with the PDV results for these particular data points in comparison to LASNEX that simulated a centerline pressure of 32 GPa at $t_{hydro} = 31\ ns$ for 200-μm-thick copper foils. At the time of writing this thesis, there were no LASNEX simulations for 50-μm-thick copper or titanium foils, and thus are omitted.

Titanium simulations differ somewhat from PDV measurements. For 200-μm-thick titanium, PDV measured a pressure of 21 GPa at $t_{hydro} = 33\ ns$, while HELIOS-CR simulated a pressure of 12.3 GPa at $t_{hydro} = 36\ ns$. The hydrodynamic disassembly times across the titanium foils agree fairly well between the simulation and experiment. However, simulated pressures differ greatly than what is calculated from the PDV measurements. This could be due to an inaccurate Ti EOS model used in HELIOS-CR, and leaves further exploration with updated EOS models.

Table 4.9 summarizes the hydrodynamic values for Al, Ni, and C from PDV and HELIOS-CR. This preliminary data does not have LASNEX simulations included. Overall, the HELIOS-CR simulations are comparable to the PDV measurements for 100-μm-thick foils of Al and Ni. The PDV measured an inferred pressure of 8 GPa at $t_{hydro} = 21\ ns$, while the simulated pressure reached 9.8 GPa at $t_{hydro} = 17\ ns$ for Al. Ni reached an inferred PDV pressure of 30.5 GPa at $t_{hydro} = 19\ ns$, while simulated Ni reached a pressure of 28.9 GPa at $t_{hydro} = 18\ ns$. However, carbon hydrodynamic values differed greatly between simulation and the experiment. The pyrolytic C PDV inferred pressure reached 3.6 GPa at $t_{hydro} = 42\ ns$, but the simulation resulted in a pressure of 11 GPa at $t_{hydro} = 19\ ns$. This could result from a multitude of effects including the low deposited energy, or the EOS model used in HELIOS-CR.

Table 4.8 (a): Summary of the hydrodynamic values from PDV and simulations for Cu.

Data Acquisition	Thickness (μm)	t_{hydro} (ns)	<P> @ t_{hydro} (GPa)
PDV	50	25	11
	100	31	18
	200	40	24
HELIOS-CR	50	21	10.6
	100	27	15.8
	200	38	24.8
LASNEX	50	-	-
	100	22	16.2
	200	31	32

Table 4.8 (b): Summary of the hydrodynamic values from PDV and simulations for Ti.

Data Acquisition	Thickness (μm)	t_{hydro} (ns)	<P> @ t_{hydro} (GPa)
PDV	50	25	12
	100	26	17
	200	33	21
HELIOS-CR	50	24	7
	100	28	8.9
	200	36	12.3
LASNEX	50	-	-
	100	20	7.6
	200	30	15.8

Table 4.9: Summary of the hydrodynamic values from PDV and simulations for 100-μm-thick C, Al, and Ni.

	PDV		HELIOS-CR	
Element	t_{hydro} (ns)	<P> @ t_{hydro} (GPa)	t_{hydro} (ns)	<P> @ t_{hydro} (GPa)
Pyrolytic C	42	3.6	19	11
Al 1100	21	8	17	9.8
Ni	19	30.5	18	28.9

CHAPTER FIVE – CONCLUSIONS AND RECOMMENDATIONS

The following document outlines the process of characterizing warm dense foils during energy deposition with the PDV diagnostic and hydrodynamic simulation. The PDV probe provides instantaneous measurements of particle velocity, foil displacement at the edge, and is used to infer the pressure in the elastic limit for a variety of foil materials. The hydrodynamic quantity of pressure, along with temperature and density, describe the EOS of materials that relate the functions of state under a given set of physical conditions. These hydrodynamic studies support the mission of DARHT, and provides insight into beam-target interactions to optimize Bremsstrahlung production and radiographic quality. DARHT Axis-1 produces large homogenous volumes of long-lasting (~100's of ns) WDM, and provides the ability to benchmark hydrodynamic codes and equation of state measurements.

In conclusion, the particle velocity, inferred pressure, and the hydrodynamic disassembly time are proportional to the target thickness for copper and titanium. However, the relationship between t_{hydro} and the foil thickness does not vary linearly as described by equation 4.1, and PDV measurements with thicker foils (>500 μm) would aid in describing the relationship. The PDV diagnostic yields the approximate electron and ion temperature of copper plasma after it hydrodynamically disassembles. It is also shown that T_e increases as energy deposition continues and with foil thickness. Measurements also suggest that the WDM experiments operate in a two-temperature regime ($T_i \neq T_e$). Additionally, the material of the target plays a significant role on the hydrodynamic behavior during energy deposition. This preliminary data on the material effect provides further benchmarking scenarios in the hydrodynamic simulations.

The 1-D hydrodynamic code HELIOS-CR models the foil targets during energy deposition with the recently added electron beam capability. HELIOS-CR and LASNEX codes simulate the beam-target interactions, and the resulting hydrodynamic values are extracted and compared to the experimental PDV values with reasonable agreements. HELIOS-CR explores the thickness and material effect on t_{hydro}, yielding a linear relationship as described in equation 4.1 for copper and titanium. Simulations in HELIOS

suggest the electron temperature in Cu foils varies by a small amount as a function of foil thickness. The initial heating stage in HELIOS-CR is valid, but simulation of the targets after disassembly needs further exploration.

The project objectives in section 1.2 includes the extraction of hydrodynamic values during energy deposition of the target foils, simulation of the results in the hydrodynamic codes, and benchmarking the simulations for future applications. Each of these objectives are met with confidence, and the groundwork for future studies has been established.

It is recommended that further parametric studies on the thickness effect on t_{hydro} should include foils of greater thickness (>500 μm) in order to better understand the relationship between Δz and t_{hydro}. Furthermore, the hydrodynamic simulations in HELIOS-CR should be explored with updated EOS and optical property tables. This may bridge the gap in understanding the foil simulations after disassembly. Quantification of n_e and T_e during the warm dense phase would provide the ability to benchmark existing EOS models. Diagnostics currently being tested and fielded on DARHT Axis-1 include interferometry, UV and X-ray spectroscopy for the measurement of these hydrodynamic values.

BIBLIOGRAPHY

1. A.B. Zylstra, J.A. Frenje, P.E. Grabowski, C.K. Li, G.W. Collins, P. Fitzsimmons, S.H. Glenzer, F. Graziani, S.B. Hansen, S.X. Hu, M. Gatu Johnson, P. Keiter, H. Reynolds, J.R. Rygg, F.H. Séguin, and R.D. Petrasso, *Measurement of Charged-Particle Stopping in Warm Dense Plasma.* Physical Review Letters, 2015. **114**.
2. F. Graziani, M.P. Desjarlais, R. Redmer, and S.B. Trickey, *Frontier and Challenges in Warm Dense Matter.* 2014.
3. G. Logan, R. Davidson, J. Barnard, and R. Lee, *A Unique U.S. Approach for Accelerator-Driven Warm Dense Matter Research - Preliminary Report.* 2004.
4. J. Daligault, *On the quantum Landau collision operator and electron collisions in dense plasmas.* Physics of Plasmas, 2016. **23**(3).
5. B.I. Cho, K. Engelhorn, A.A. Correa, T. Ogitsu, C.P. Weber, H.J. Lee, J. Feng, P.A. Ni, Y. Ping, A.J. Nelson, D. Prendergast, R.W. Lee, R.W. Falcone, and P.A. Heimann, *Electronic Structure of Warm Dense Copper Studied by Ultrafast X-Ray Absorption Spectroscopy.* Physical Review Letters, 2011. **106**.
6. B.I. Cho, T. Ogitsu, K. Engelhorn, A.A. Correa, Y. Ping, J.W. Lee, L.J. Bae, D. Prendergast, R.W. Falcone, and P.A. Heimann, *Measurement of Electron-Ion Relaxation in Warm Dense Copper.* Scientific Reports, 2016. **6**.
7. W. Bang, B.J. Albright, P.A. Bradley, E.L. Vold, J.C. Boettger, and J.C. Fernández, *Uniform heating of materials into the warm dense matter regime with laser-driven quasimonoenergetic ion beams.* Physical Review E, 2015.
8. A. Pelka, G. Gregori, D. O. Gericke, J. Vorberger, S. H. Glenzer, M. M. Günther, K. Harres, R. Heathcote, A. L. Kritcher, N. L. Kugland, B. Li, M. Makita, J. Mithen, D. Neely, C. Niemann, A. Otten, D. Riley, G. Schaumann, M. Schollmeier, An. Tauschwitz, and M. Roth, *Ultrafast Melting of Carbon Induced by Intense Proton Beams.* Physical Review Letters, 2010. **105**.
9. W. Bang, B. J. Albright, P. A. Bradley, D. C. Gautier, S. Palaniyappan, E. L. Vold, M. A. Santiago Cordoba, C. E. Hamilton and J. C. Fernández, *Visualization of expanding warm dense gold and diamond heated rapidly by laser-generated ion beams.* Scientific Reports, 2015. **5**.

10. J.E. Coleman and J. Colgan, *Spatially and temporally resolved measurements of a dense copper plasma heated by intense relativistic electrons.* Physics of Plasmas, 2017. **24**.
11. S.H. Glenzer, *X-ray Thomson Scattering in High Energy Density Plasmas.* Rev. Mod. Phys., 2009.
12. J.E. Coleman and J. Colgan, *Collisional heating and adiabatic expansion of warm dense matter with intense relativistic electrons.* Physical Review E, 2017. **96**.
13. C. Ekdahl, *Electron beam dynamics in the long-pulse, high-current DARHT-Il linear induction accelerator.* Particle Accelerator Conference, 2009.
14. T.J. Burris-Mog and D.C. Moir, *Quantifying spot size reduction of a 1.8 kA electron beam for flash radiography.* J. Appl. Phys. , 2018. **123**.
15. M.J. Burns, P.W. Allison, R.L. Carlson, J.N. Downing, D.C. Moir, and R.P. Shurter, *Status of The Dual-Axis Radiographic Hyrdotest Facility.* Los Alamos National Laboratory.
16. B.T. McCuistian, D.C. Moir, E. Rose, H. Bender, C. Carlson, C. Hollabaugh, and R. Trainham, *Temporal Spot Size Evolution of the DARHT First Axis Radiographic Source.* Proceedings of EPAC08, 2008.
17. S. Nath, *Linear Induction Accelerators at The Los Alamos National Laboratory DARHT Facility.* Proceedings of LINAC2010, 2010.
18. J. Fockler, B. Bowen, V. Carboni, P. Corcoran, J. Kishi, and R. Kuenning, Proceedings of the Eighth IEEE International Pulsed Power Conference, 1991.
19. J. Downing, W. M. Parsons, L. M. Earley, J. G. Melton, D. C. Moir, R. L. Carlson, G. A. Barnes, L. A. Builta, S. A. Eversole, G. Keel, D. C. Rader, J. A. Romero, and R. P. Shurter, Proceedings of the Eighth IEEE International Pulsed Power Conference, 1991.
20. J.E. Coleman, H.L. Andrews, J.P. Colgan, M.S. Jakulewicz, J.O. Perry, N.B. Ramey, T. Schmidt, D.R. Welch, and C.L. Miller, *Isochoric Heating and Adiabatic Expansion of WDM with Intense Relativitic Electrons.* APS Talk, 2017.

21. J.E. Coleman, D.C. Moir, M.T. Crawford, D.R. Welch, and D.T. Offerman, *Temporal Response of a Surface Flashover on a Velvet Cathode in a Relativistic Diode.* Physics of Plasmas, 2015. **22**.
22. J.E. Coleman, D. C. Moir, C. A. Ekdahl, J. B. Johnson, B. T. McCuistian, and M. T. Crawford, Proceedings of the 2013 IEEE Pulsed Power and Plasma Science Conference, 2013.
23. M. Burns, P. Allison, L. Earley, D. Liska, C. Mockler, J. Ruhe, H. Tucker, L. Walling *Cell Design for the DARHT Linear Induction Accelerators.* IEEE 1991.
24. J.E. Coleman, D. C. Moir, C. A. Ekdahl, J. B. Johnson, B. T. McCuistian,G. W. Sullivan, and M. T. Crawford, *Increasing the intensity of an induction accelerator and reduction of the beam breakup instability.* Physical Review Special Topics - Accelerators and Beams, 2014. **17**.
25. *Stopping-Power and Range Tables for Electrons.* NIST Database, See physics.nist.gov/cgi-bin/Star/e_table.pl for information about dE/dx.
26. See http://periodictable.com for Latent Heat Values.
27. See http://www.lenntech.com/periodic/periodic-chart.htm for Ionization Energies.
28. P. Forck, P. Kowina, and D. Liakin, *Beam Position Monitors.* CERN Accelerator School, 2008.
29. B. Gitter, *Optical Transition Radiation.* UCLA Department of Physics Center for Advanced Accelerators, 1992.
30. L.M. Barker and R.E. Hollenbach, *Laser interferometer for measuring high velocities of any reflecting surface.* Journal of Applied Physics, 1972. **43**.
31. O.T. Strand, D.R. Goosman, C. Martinez, and T.L. Whitworth, *Compact system for high-speed velocimetry using heterodyne techniques.* Review of Scientific Instruments, 2006. **77**.
32. J.E. Coleman, H.E. Morris, M.S. Jakulewicz, H.L. Andrews, and M.E. Briggs, *Hydrodynamic disassembly and expansion of electron-beam-heated warm dense copper.* Physical Review E, 2018. **98**.

33. J.J. MacFarlane, I.E. Golovkin, and P.R. Woodruff, *HELIOS-CR - A 1-D Radiation-Magnetohydrodynamics Code with Inline Atomic Kinetics Modeling.* Prism Computational Sciences.

34. J.E. Bailey, G.A. Chandler, S.A. Slutz, G.R. Bennett, G. Cooper, J.S. Lash, S. Lazier, R. Lemke, T.J. Nash, D.S. Nielsen, T.C. Moore, C.L. Ruiz, D.G. Schroen, R. Smelser, J. Torres, and R.A. Vesey, *X-ray imaging measurements of capsule implosions driven by a Z-pinch dynamic hohlraum.* Physical Review Letters, 2002. **89**(9).

35. J.J. MacFarlane, I.E. Golovkin, R.C. Mancini, L.A. Welser, J.E. Bailey, J.A. Koch, T.A. Mehlhorn, G.A. Rochau, P. Wang, and P. Woodruff, *Dopant radiative cooling effects in indirect-drive Ar-doped capsule implosion experiments.* Physical Review E, 2005. **72**(6).

36. *Prism Opacity and Equation of State Code.* Prism Computational Sciences. See http://www.prism-cs.com/Software/Propaceos/overview.html for information on PROPACEOS.

37. *SESAME: The Los Alamos National Laboratory Equation of State Database.* See https://permalink.lanl.gov/object/tr?what=info:lanl-repo/lareport/LA-UR-92-3407 for information on SESAME.

38. G. Zimmerman, D. Kershaw, D. Bailey, and J. Harte, *The LASNEX code for inertial confinement fusion.* For Presentation at the ICF Conference, 1977.

39. S.P. Marsh, *Los Alamos Series on Dynamic Material Properties.* University of California Press, 1980.

40. R.P. Drake, *High-Energy-Density Physics: Foundation of Inertial and Experimental Astrophysics.* Springer, New York, 2017.

41. J.D. Huba, *NRL Plasma Formulary.* The Office of Naval Research, 2016.

VITA

Payson Dieffenbach grew up in a small town in Southern Indiana known only for its historic natural springs and for a famous basketball player who also originated there, Larry Bird. Sometime in middle school, Payson recognized the power of the atom, and became fascinated with the work of nuclear engineers. He became focused on his academics in high school, and applied to a single college in the state of Indiana, Purdue University to study Nuclear Engineering. Here he became enthralled in his studies and adapted to the college environment fairly easily. During his sophomore year, he gained an interview with a reputable company in nuclear energy generation, but did not receive the opportunity to intern in the end. He searched for another opportunity for the summer, and was recommended undergraduate research for a group known as the Center for Materials Under eXtreme Environments. He spent two years working as an undergraduate research assistant in the laser-material interactions subgroup, while simultaneously keeping up with his social and academic life. Succeeding in his academics, he searched and applied for graduate schools to continue his education in the field of Nuclear Engineering, where he was accepted to The University of Tennessee – Knoxville under Dr. David Donovan. During Payson's first year, he was introduced to Dr. Josh Coleman at Los Alamos National Laboratory, and to the work that this thesis is based on. If you can't find Payson on campus working on something, you can usually find him relaxing in his apartment with his girlfriend, Robin, and their two cats, Dingle and Boo.